Polymer Bulletin (2022) 79:7827–7842
https://doi.org/10.1007/s00289-021-03872-x

ORIGINAL PAPER

Original polymer P-DSBT nano-composite with ZnO nanoparticles for gas sensor at room temperature

Mehdi Akermi[1,2] · Nejmeddine Jaballah[2] · Yahya Alajlani[1] · Montassar Najari[3] · Rafik Ben Chaabane[2] · Hafedh Ben Ouada[2] · Mustapha Majdoub[2]

Received: 8 March 2021 / Revised: 25 May 2021 / Accepted: 26 August 2021 /
Published online: 12 September 2021

Abstract

Recently, polymer composite material has shown excellent performance in a wide range of technological applications, such as renewable energy, biomedical applications, optoelectronic devices …etc. As the knowledge-base on this emergent material continues to grow, a new kind of hybrid sensors fabricated with semiconducting metal oxides and conducting polymers had been synthesized and had demonstrated high sensing capability for several poisonous gases and chemical warfare agents at room temperature. This research work introduces the synthesis and the characterization of a novel polymer **P-DSBT** composite consisting of ZnO nanoparticles (**P-DSBT/ZNO**). The composite films **P-DSBT/ZNO** are prepared by spin coating technique and then studied using different spectroscopic characterization techniques, i.e., FTIR, XRD, SEM, TEM, AFM and UV–Vis to further investigate on the structure and the morphology of this material. For assessing the P-DSBT/ZNO selectivity, different oxidizing and reducing gases were applied and it was found that the nanocomposite has the best selectivity for methane (CH_4). The obtained **P-DSBT/ZNO** shows a wide sensing range (0–200 ppm) and a very high response magnitude, i.e., relative resistance changes of approximately 40% per 60 ppm of CH_4. The key finding of this work is that sensitivity for gas detection is greatly improved by the interaction of ZnO-based hybrid materials at room temperature.

Keywords Nanocomposites · ZnO · Polymer · Gas sensor · Room temperature

✉ Mehdi Akermi
makermi@jazanu.edu.sa

[1] Department of Physics, Faculty of Science, Jazan University, Jazan 45142, Saudi Arabia

[2] Laboratory of Interfaces and Advanced Materials, Faculty of Science, University of Monastir, Boulevard of the Environment, 5019 Monastir, Tunisia

[3] Innovation and Entrepreneurship Centre IEC, Jazan University, Jazan 45142, Saudi Arabia

Introduction

In recent years, the interest in the study of nanocomposite polymer system has been continuously developing due to their various potential applications in sensors and dielectrics [1]. Different researcher teams suggested that the addition of inorganic nanoparticle into polymers results in an upgraded polymer property that importantly contrasts from the properties of conventional polymer [2, 3]. It has been discovered that the inorganic nanoparticle expressively influences the properties of base polymers when they are introduced to it to form what it's called a nanocomposite [4]. In this context, there is an increasing need for development of a highly sensitive and selective CH_4 gas sensor that can sense at low concentrations (ppm/ppb). Various semiconducting metal oxides, such as ZnO, SnO_2, WO_3 and others [5, 6], and semiconductor polymer, such as polythiophene (PTH), polyaniline (PANI) and polypyrrole (PPY), are similarly being considered for gas sensing [7] and optoelectronic applications [8]. These materials are also being investigated, as they have distinct advantages of easy production, low cost and room temperature processing. Among organic materials, polythiophene is a p-type material and has attracted much interest because of room temperature operation, chemical stability against atmospheric conditions, excellent conductivity, low cost, structural flexibility [9–11], easy process ability, convenient processing, tunable electronic properties, efficient luminescence, structural flexibility and its semiconducting potential and even its metallic behavior [12, 13].

Among the different strategies for the fabrication of selective and low temperature effective gas sensor, the combination of nanostructured metal oxides with conducting polymers (nanocomposite) remains among the most attractive strategies [14]. Progress in hybrids organic–inorganic encompasses development of many industries, such as the aerospace industry, manufacturing machine parts with high performance, and manufacturing medicine. Hybrids organic–inorganic are a special class of materials formed by combination of two or more nano-sized objects or nanoparticles, resulting in materials having unique physical properties compared with single material [15]. Organic–inorganic nanocomposites are the new class of materials receiving growing research interests in recent years due to their improved optical and electrical properties [16]. Such nanocomposites are an advanced system because of strong electronic interaction between the individual components and can be immediately hybridized on a molecular level [17–26]. In the present work, an organic–inorganic hybrid nanocomposite containing a novel sulfur-containing polymer was prepared based on the p-conjugated distyrylbithiophene system as an organic material. This organic material was prepared via Wittig polycondensation and zinc oxide (ZnO) as an inorganic substance [27]. The ZnO nanoparticles are added in the distyrylbithiophene matrix in different weight percentages (10–100%), and hybrid nanocomposite films were prepared by spin casting on ITO substrate. The compositional analysis was carried out by ultraviolet–visible (UV–Vis) spectrophotometry. The interaction between distyrylbithiophene and ZnO nanoparticles was explored by atomic force microscopy (AFM) and contact angle measurement. The impedance characteristics of the

nanocomposite **P-DSBT/ZnO** was studied under different gas concentrations at room temperature. The nanocomposite **P-DSBT/ZnO** conductance was investigated using methane and measured by a Keitley 4192 A PACKARD/voltage source. The remainder of this paper is structured as follows: Sect. "Material and Methods" presents the used materials and methodology to develop the nanocomposite **P-DSBT/ZnO**. Section "Results and discussions" then presents experimental results and further discussions. Finally, Sect. "Conclusion" gives conclusions and future work.

Material and methods

Synthesis of P-DSBT polymer

The sulfur-containing polymer (P-DSBT) was synthesized via the witting poly-condensation as shown in Fig. 1. To a stirred equimolar mixture of 1,1′-thiobis (4-ethoxy-3-triphenylphosphoniomethylbenzene) dichloride (1 mmol) and 5,50-diformyl-2,20-bithiophene (1 mmol) in 10 mL of anhydrous THF, 10 ml of a 0.5 M t-BuOK solution in THF (5 mmol) was added dropwise at room temperature under an argon atmosphere. The reaction mixture was stirred for 24 h after the addition and then acidified with 3% aqueous hydrochloric acid, poured into water, and extracted with chloroform. The organic phase was washed with water, concentrated, and then precipitated from methanol. Further purification of the polymer was carried out by several precipitations in methanol from chloroform solution [28].

Synthesis of zinc oxide (ZnO) nanoparticles

The synthesis of zinc oxide nanostructures was conceded out using zinc acetate dehydrate and sodium hydroxide as precursors. An aqueous solution of zinc acetate (0.2 M) was equipped. The solution pH was attuned to 9.5 by adding NaOH. After reaching pH-9.5, the colloidal solution was left stirring for 2 h. Then, white precipitate was separated by centrifugation at a speed of 3000 rpm for 20 min at room temperature. Several extractions, coating with water and ethanol were implemented after every centrifugation to eliminate sodium acetate. Finally, the powders were annealed at 310 1C for 10 h [27].

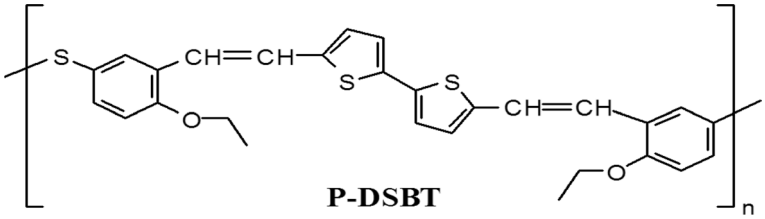

P-DSBT

Fig. 1 Chemical structure of P-DSBT (sulfur-containing polymer)

Synthesis of P-DSBT–ZnO hybrid nanocomposites

Mechanical mixing method was employed for preparation of **P-DSBT**–ZnO hybrid nanocomposites. Nano-crystalline ZnO powder was added to **P-DSBT** matrix in different weight percentages (10–100 wt %). The obtained powder was dissolved in chloroform solvent and stirred for 2 h with the help of a magnetic stirrer to obtain a sulfur-containing polymer–ZnO hybrid casting solution. The resultant casting solution was used for the preparation of sulfur-containing polymer/ZnO hybrid nanocomposites films. The films were prepared on ITO substrate (10*10 mm^2) by simple and cost-effective spin coating method. After the thin layers of ZnO/polymer were elaborated in different percentages, a series of characterization of the devices was applied in the remainder of this work.

Results and discussions

FTIR spectroscopy

Figure 2 shows the nanostructure IR spectrum (ZnO powders) which was acquired in the range of 400–4000 cm^{-1} for the powders calcined at 300 °C. Absorption bands near 3500 cm^{-1} represent O–H mode of vibration, those at 2938 cm^{-1} are C-H stretching mode and those at 1400–1600 cm^{-1} are the C=O stretching mode. The band arising from the absorption of atmospheric CO_2 on the metallic cations at 2350 cm^{-1} and bonding between Zn–O (400 cm^{-1}, 550 cm^{-1}) are also visible [29].

Figure 3 shows the FT-IR spectrum of the polymer (P-DSBT) which was acquired on a Perkin-Elmer BX FT-IR system spectrometer (by dispersing samples in KBr disks). Absorption bands 3062, 3037 (w, aromatic and vinylic C–H stretching), 2976, 2925, 2877 (w, aliphatic C–H stretching), 1617, 1583 (m, C=C stretching), 1488, 1470 (aliphatic C–H asymmetric bending), 1391 (aliphatic CH

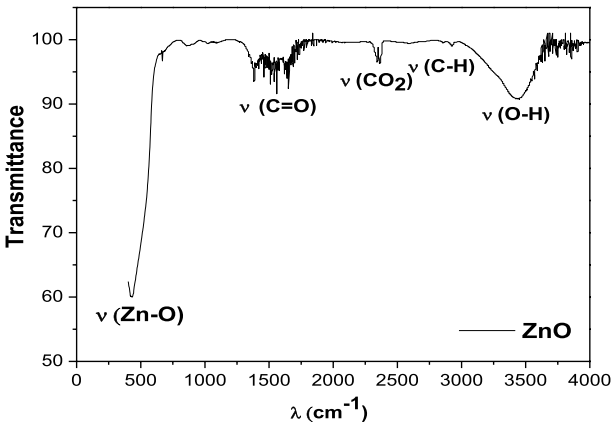

Fig. 2 FTIR spectrum of the ZnO nanostructure

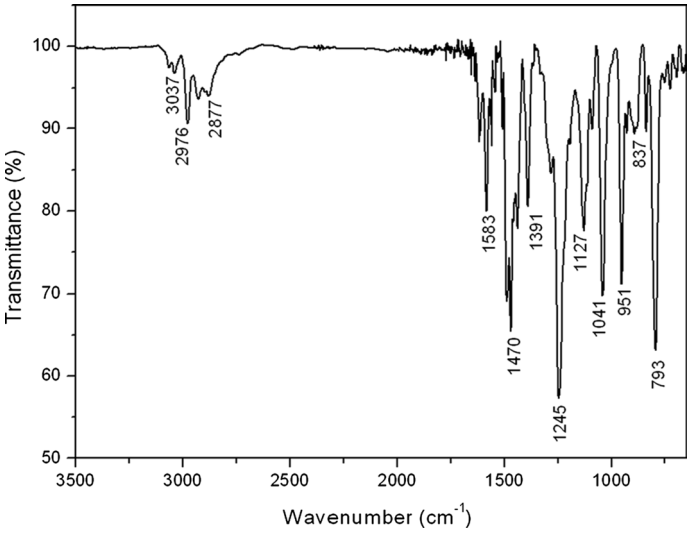

Fig. 3 FT-IR spectrum of the polymer (KBr)

symmetric bending), 1245 (s, C–O–C asymmetric stretching), 1041 (m, C–O–C symmetric stretching), 793 (s, aromatic C–H out-of-plane bending), 951 (m, trans-HC=CH out-of-plane bending), 837 (w, cis–HC=CH out-of-plane bending).

Analysis by X-ray diffraction

The crystal structure of ZnO nanoparticles was characterized by X-ray diffractometer equipped with a monochromated CuKa (l ¼ 1:54,249 A) radiation. Nanoparticles (XRD) patterns recorded from 28 to 71 in 2θ are shown in Fig. 4. All peaks present in the diffractograms have been indexed according to the hexagonal wurtzite structure of ZnO. Thus, we can conclude that the powders obtained are well crystallized. The thermodynamically stable phase for ZnO is the wurtzite structure in the hexagonal crystal system, although two other metastable cubic phases may exist as well, namely zinc blende and high-pressure rock-salt. In [30], the quartzite crystal structure features noncentrosymmetric symmetry and polar surfaces and is best described as alternating planes composed of tetrahedral coordinated Zn^{2+} and O^{2-} ions stacked along the c-axis. The main significant peaks for ZnO film were found to be (100), (002), (101), (102) and (110), (103), (200), (112) and (201). The crystalline size was evaluated from the XRD data. The width of the Bragg peak is a combination of both instrument- and sample-dependent effects. In order to dissociate these contributions, diffraction pattern was collected from the line broadening of a standard material, silicon, to determine the instrumental broadening [31]. The corrected instrumental broadening $\beta_{Si} = 0.073$ rad; β_{hkl} corresponding to the diffraction peak of ZnO was estimated by using Eq. 1 [32]:

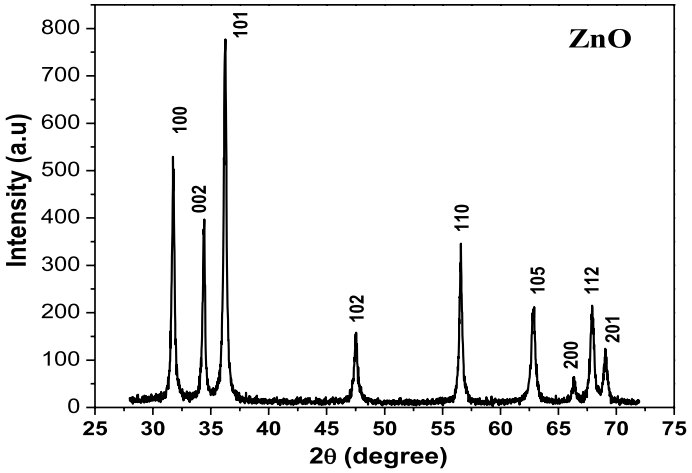

Fig. 4 **X**-ray diffraction (XRD) pattern of synthesized nanostructure ZnO powder

$$\beta_{hkl} = \left[\left(\beta_{hkl}\right)^2_{measured} - \left(\beta^2_{instrumetale}\right) \right]^{\frac{1}{2}} \quad (1)$$

The crystallite size of the ZnO was determined from β_{hkl} of (1 0 1) diffraction peak using the Scherrer formula:

$$D = \frac{0.94\lambda}{\beta_{hkl} cos\theta} \quad (2)$$

where D, λ, θ and β are the mean grain size, the x-ray wavelength and the Bragg diffraction angle of the (101) peak, respectively. The XRD pattern of the sample indicates enhanced intensity for the peak corresponding to (101) plane, indicating preferential orientation along the c-axis. The crystallite size was found to be (36 ± 0.23) nm.

Figure 5a, b shows the representative SEM and TEM images of the obtained ZnO material. In these figures, quite characteristic morphologies of the as-synthesized ZnO structures are observed, i.e., aggregated ZnO nanoparticles of spherical shape with a dimension of ten nanometers.

AFM analysis

The two-dimensional (2D) surface topography of **P-DSBT**–ZnO (10–100%) hybrid nanocomposite was investigated using atomic force microscopy (AFM). Figure 6 shows the AFM images in scanning mode of the polymer alone (Fig. 6a), the ZnO alone (Fig. 6b) and of the **P-DSBT**–ZnO hybrid films deposited on the ITO substrates. There is a large difference between the different films. Images corresponding to the films with ZnO concentrations in the 10%, 20% and 40% (Fig. 6c–e) in

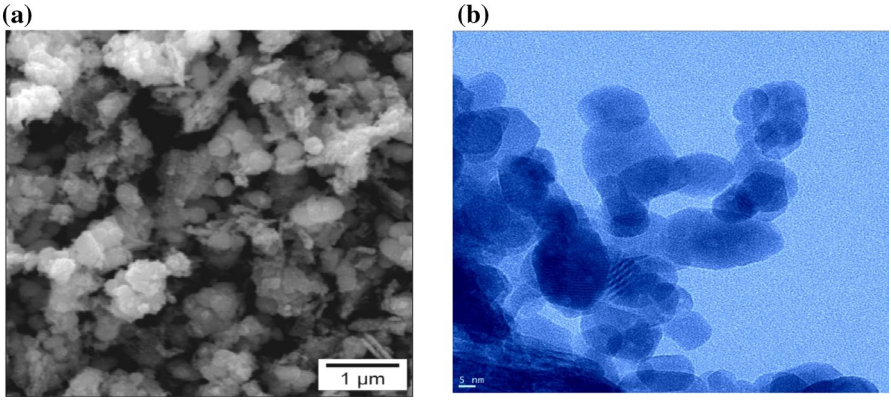

Fig. 5 SEM **a** and TEM **b** images of nanostructure ZnO

P-DSBT indicate that the dispersion of the nanoparticles in the **P-DSBT** is better (more uniform) than higher concentrations (> 40%). On the other hand, for higher ZnO concentrations (40%, 50% and 100%), there is the formation of aggregates embedded in the matrix as it is shown in Fig. 6e–g. The root-mean-square (RMS) roughness of the hybrid films increases as a function of the percentages of ZnO in the matrix, which is attributed to the incorporation of ZnO in the **P-DSBT** (ZnO(10%): 0.955 nm, ZnO(20%): 0.960 nm, ZnO(40%): 0.965 nm, ZnO(50%): 1.448 nm, ZnO(100%): 1.448 nm, 1.842). Also, AFM images (Fig. 6) exhibit spherical elongated structures with disconnected channels indicating an increase in roughness of the surface. The rough surface is a positive factor for the performance of the gas sensor due to a larger contact surface with the active layer [33].

Ultraviolet–Visible (UV–Vis) spectroscopy study

To understand the effect of addition of ZnO nanoparticles in **P-DSBT** matrix, the Ultraviolet–visible (UV–Vis) spectroscopy was carried out. Figure 7a shows the UV–Vis spectra of **P-DSBT, ZnO** and **P-DSBT/ZnO** hybrid nanocomposites. **P-DSBT** film shows a broad absorption peak at 432 nm and ZnO at 371 nm, which is in good agreement with common reported results. The **P-DSBT/ZnO** hybrid film whose maximum absorption band is located at 445 nm, therefore, exhibits a redshift with respect to the pure **P-DSBT** film. This shift is associated with the effect of ZnO nanoparticles with the presence of shorter length conjugate segments which have a lower optical gap [34]. The shift was observed for all nanocomposite films. The amount of visible range radiation absorbed by the polymer alone is higher than that of the other hybrid devices (**P-DSBT**/ZnO). Figure 7b shows that the absorbance in the visible of the various percentages of ZnO in the **P-DSBT** decreases and from 40% increases and this improvement in absorbance is explained by the formation of ZnO aggregates. Indeed, the more the concentration of ZnO increases, the more the number of photons absorbed decreases [35].

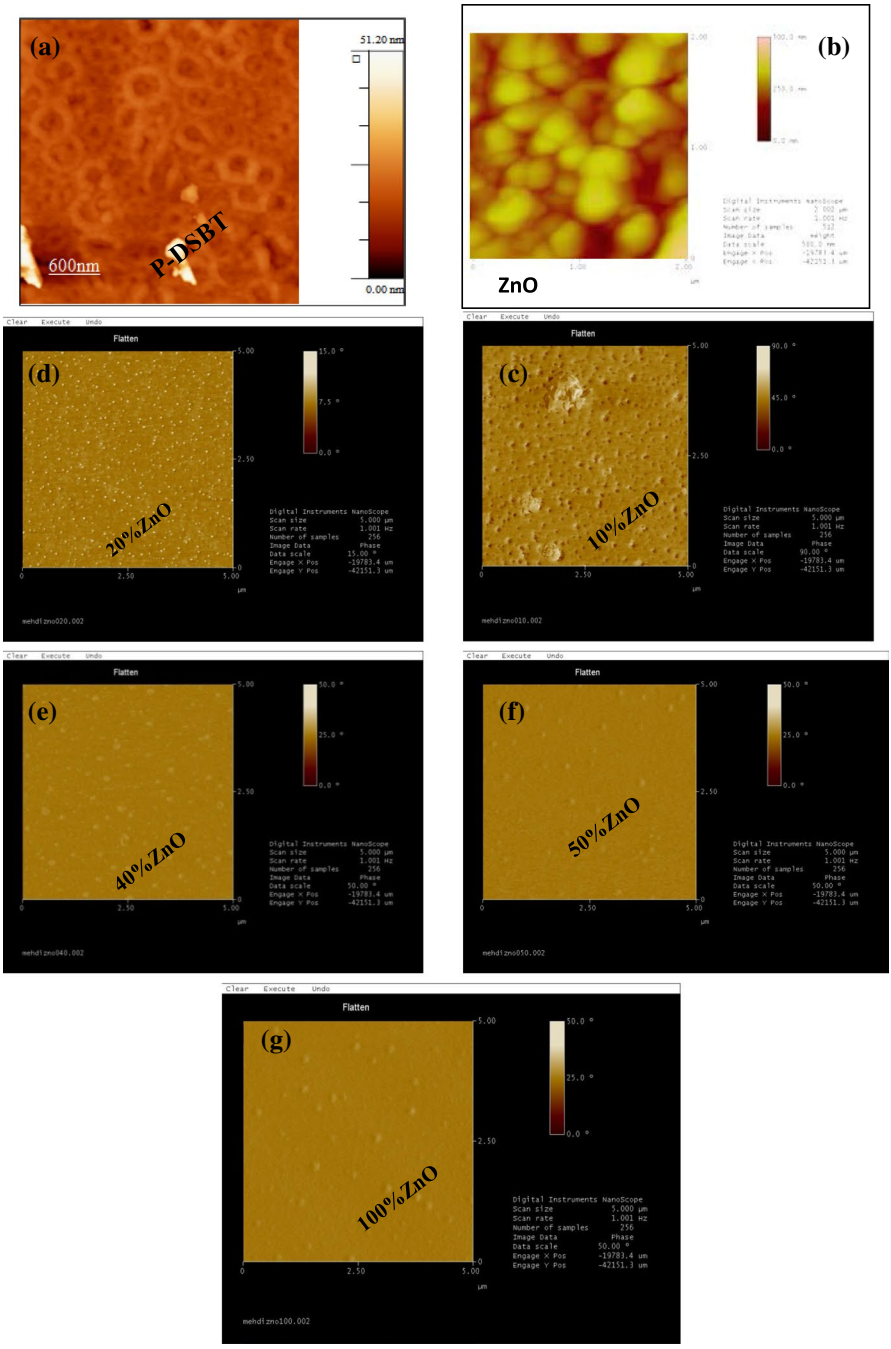

Fig. 6 AFM images of **a** P-DSBT, **b** ZnO and P-DSBT/ZnO hybrid nanocomposites with ZnO mass ratios of **c** 10%, **d** 20%, **e** 40%, **f** 50% and **g** 100%

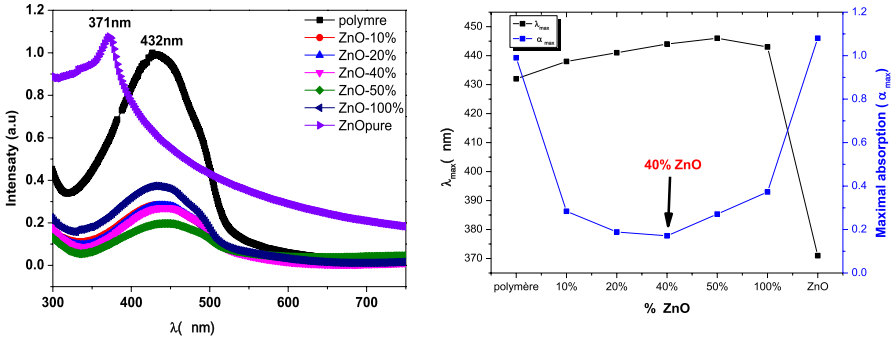

Fig. 7 **a** Variation of the UV–Vis spectra of pure P-DSBT and hybrid P-DSBT/ZnO nanocomposites for different incorporated ZnO mass ratios, **b** variation of the absorbance in visible range for different incorporated ZnO mass ratios in P-DSBT polymer

Determination of optical band gap

Optical transition in the nanocomposite films was estimated using Tauc's plot. The frequency-dependent relation of the absorption coefficient has been shown by the following relation:

$$(\alpha h\nu)^{1/n} = k(h\nu - Eg) \tag{3}$$

where α is the absorption coefficient, h is the photon energy n is the nature of electronic transition, K is the proportionality constant and Eg is the optical band gap reflected. The absorption coefficient has been calculated using Beer's Lambert law as shown by the following relation [36].

$$\boldsymbol{\alpha = -(1/d)ln(T)} \tag{4}$$

where, d is the thickness and T is the transmittance of the film. Figure 8 shows direct allowed transition between the edge of valence band and conduction band of pristine polymer P-DSBT and P-DSBT/ZnO nanocomposites. The optical band gap was obtained by extrapolation of the linear region of the corresponding curve between $\boldsymbol{(\alpha h\nu)^2}$ and $\boldsymbol{h\nu}$. The optical band gap of P-DSBT was estimated ~2.41, respectively. It was observed that there was major change in PANI/PPY/ZnO nanocomposites due to incorporation of the ZnO nanoparticle. With increase in the concentration of ZnO into P-DSBT polymeric pattern, the optical band gap decreased due to the formation of intermediate levels in between energy gap and led to increased p-type conductivity. Therefore, electron started moving from valence band to conduction band through intermediate level [37]. As a consequence, the conductivity was increased and the band gap was decreased. The optimized band gap (~2.36 eV) was observed for 40% P-DSBT/ZnO nanocomposite.

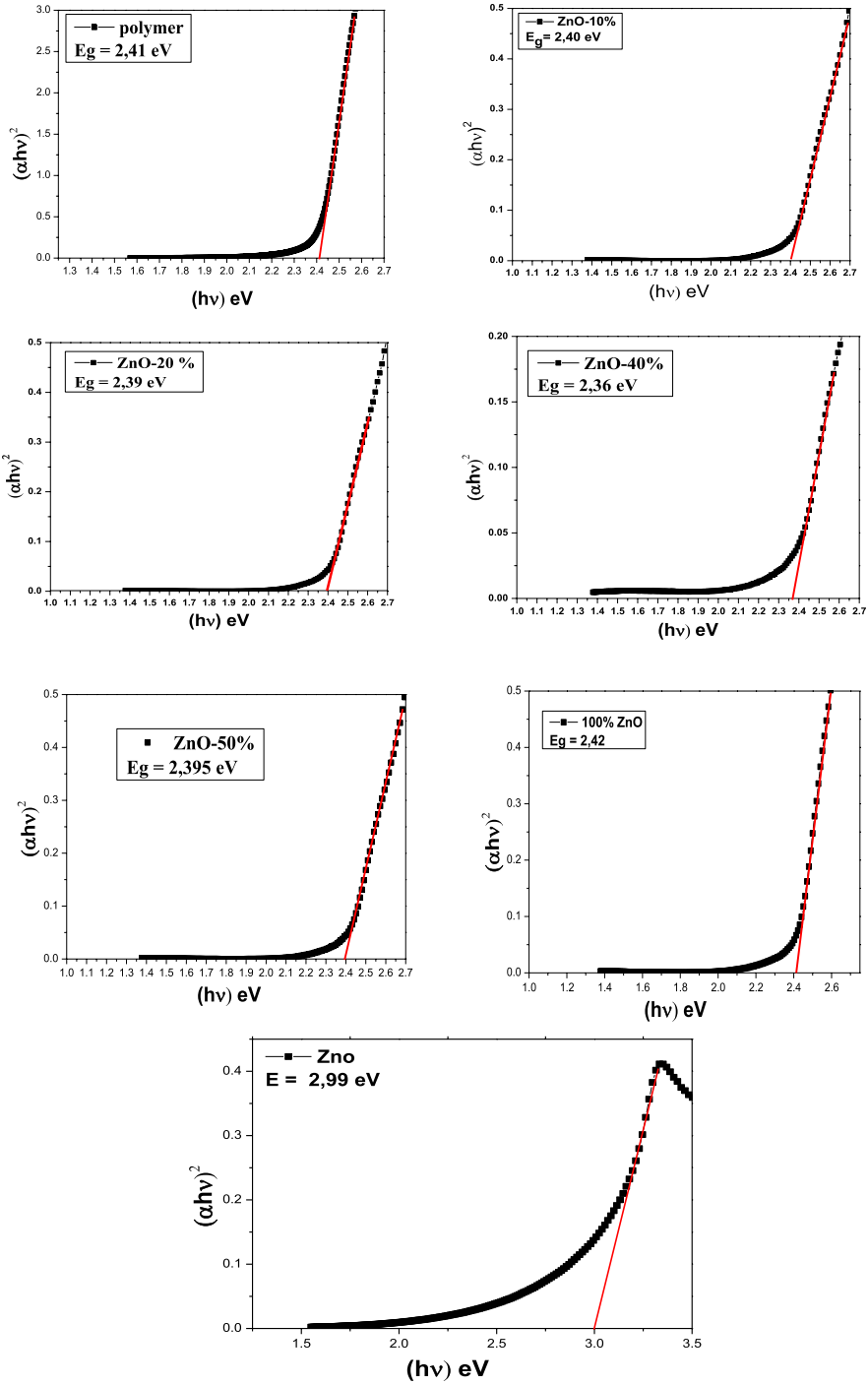

Fig. 8 Optical band gap for ZnO P-DSBT nanocomposites

Electrical properties of P-DSBT/ZnO nanocomposite: Conductance of hybrid devices in the presence of methane

Conductance study (with methane gas)

In order to evaluate the impact of the P-DSBT/ZnO nanocomposite morphological structure on sensitivity, impedance measurement was carried out using different mass ratios of ZnO with different methane gas concentrations and under a 5 V biasing voltage at room temperature. Figure 9a–e shows Nyquist diagrams for **P-DSBT/ZnO** nanocomposites made with pure polymer, pure ZnO and 4 different mass ratios of ZnO; 10%, 20% and 40%, respectively. Different concentrations

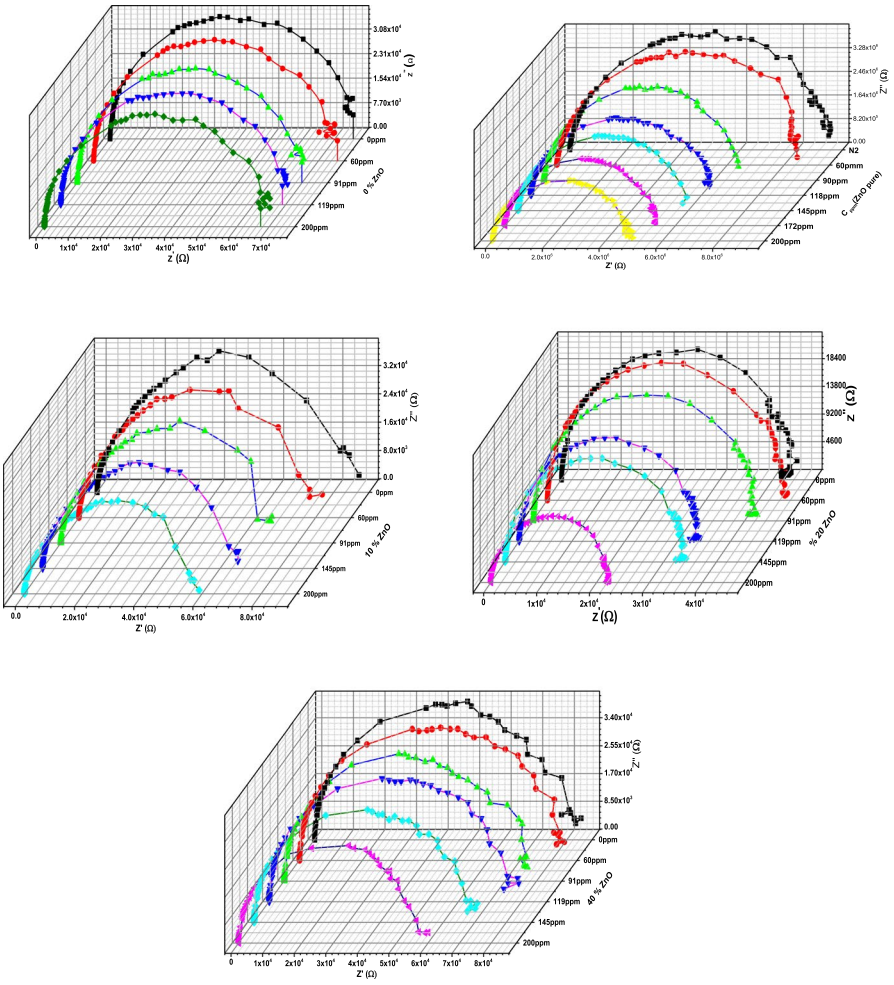

Fig. 9 The Nyquist plots of the composite P-DSBT/ZnO depending on the concentration of CH_4

of methane (60 ppm, 91 ppm, 119 ppm, 145 ppm and 200 ppm) at room temperature conditions were used.

When the concentration of gas is increased, the radius of the semicircle decreases, which means an increase in conductivity. This phenomenon is related to the injection of electrons from the methane gas and the increase in electron concentration of the sensor sensitive membrane which leads to an increase in the conductivity. Mass ratios higher than 40% higher are not considered due to their non-uniform morphological structure as explained before in Sect. "FTIR spectroscopy". The gas sensing mechanism of **P-DSBT/ZnO** hybrid nanocomposite sensor systematically investigates the terms of the formation of heterojunctions due to the existence of p-type and n-type materials [38]. It is well known that, the resistance of the sulfur-containing **P-DSBT/ZnO** hybrid nanocomposite sensor increases on exposure of CH_4 (electron donor) gas. This can be explained in terms of an energy band diagram of **P-DSBT/ZnO** hybrid nanocomposite as shown in Fig. 10a, b. Grains of semiconductor metal oxide ZnO are covered with adsorbed oxygen molecules, which capture electrons from the conduction band of the ZnO and chemisorbed oxygen species were produced which results in the formation of depletion layer on the surface region of the grains in Fig. 10c. In **P-DSBT/ZnO** hybrid nanocomposite, n-type ZnO nanoparticles form a depletion layer with p-type **P-DSBT**. When the sensor was exposed to CH_4 gas molecules, the width of the depletion layer increases resulting in an increase in resistance as shown in Fig. 10d and hence decreases in conductivity of the sensing material [39]. The adsorption of CH_4 gas molecules in **P-DSBT** matrix increases space charge region and the modulation in the space charge region at the interface of heterojunction leads to enhanced gas sensing performance of **P-DSBT/ZnO** hybrid nanocomposite sensor film.

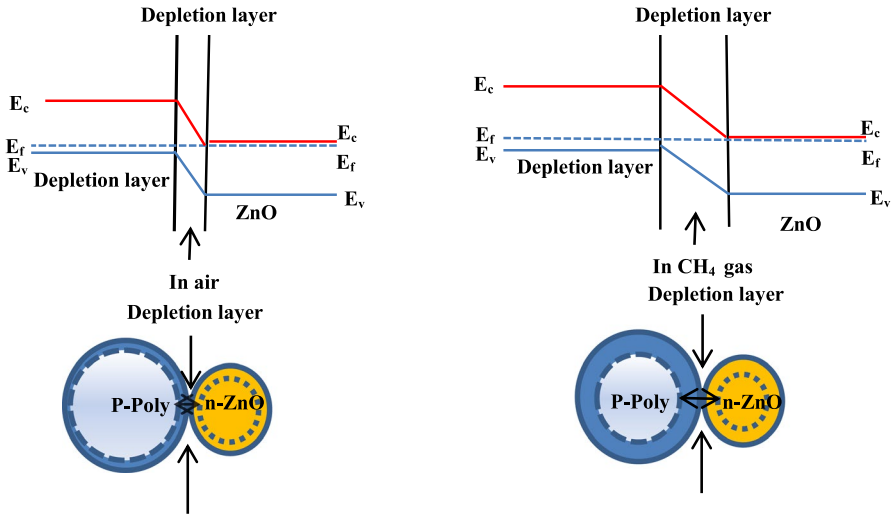

Fig. 10 Proposed schematic view of energy band diagram for P-DSBT/ZnO hybrid nanocomposites in presence of **a** air and **b** CH4 gas, schematic model for the p-type Poly-n-type ZnO heterojunction-based sensors when exposed to **c** air and **d** CH_4 gas

Sensitivity study

Sensitivity can be calculated using Eq. 5 [40]:

$$S = \frac{\left(Z''_{N_2} - Z''_{CH_4}\right)}{Z''_{N_2}} \times 100\% \quad (5)$$

where Z''_{CH4} and Z''_{N2} correspond to the maximum impedances of the imaginary part at the relaxation frequency under methane and under nitrogen in the Nyquist diagrams, respectively. The sensitivity variation with methane concentration is represented in Fig. 11 which shows the conductivity amplification with different gas concentrations at room temperature and direct 5 V biasing conditions.

Figure 11 shows sensitivity variation curves with different CH4 concentrations and for pure ZnO, pure P-DSBT polymer and P-DSBT/ZnO with different zinc oxide mass ratios (10%, 20% and 40%). The sensitivity increases as a function of methane concentration to reach values between 30 and 50%. This shows that the hybrid materials are used as a gas sensor. The different devices produced do not have the same sensitivity and, in some cases, can equal or even exceed pure ZnO sensitivity. Sensitivity variation figure can be considered as three regions (I, II and III).

Region (I) is the region related to low gas concentrations ($C_{CH4} < 90$ ppm) in which the **P-DSBT**/ZnO-40% hybrid film exhibits the best sensitivity, whereas pure ZnO doesn't (Fig. 12a). This result also shows that this type of hybrid can be used as a methane sensor for low methane concentrations.

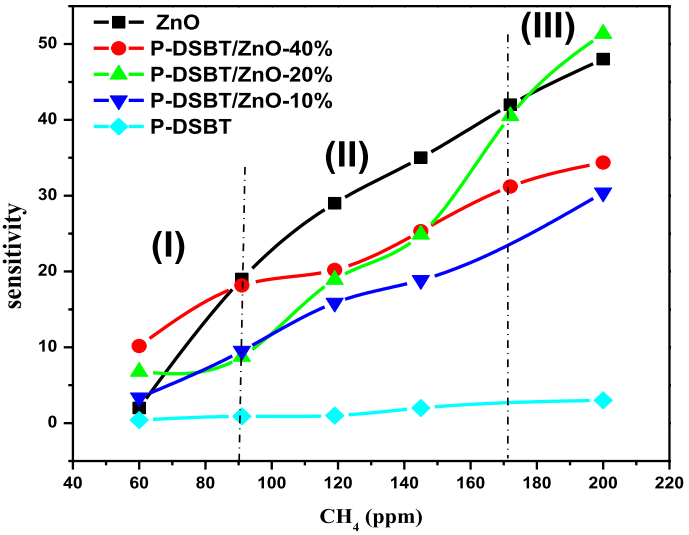

Fig. 11 Sensitivity variation with CH_4 concentration

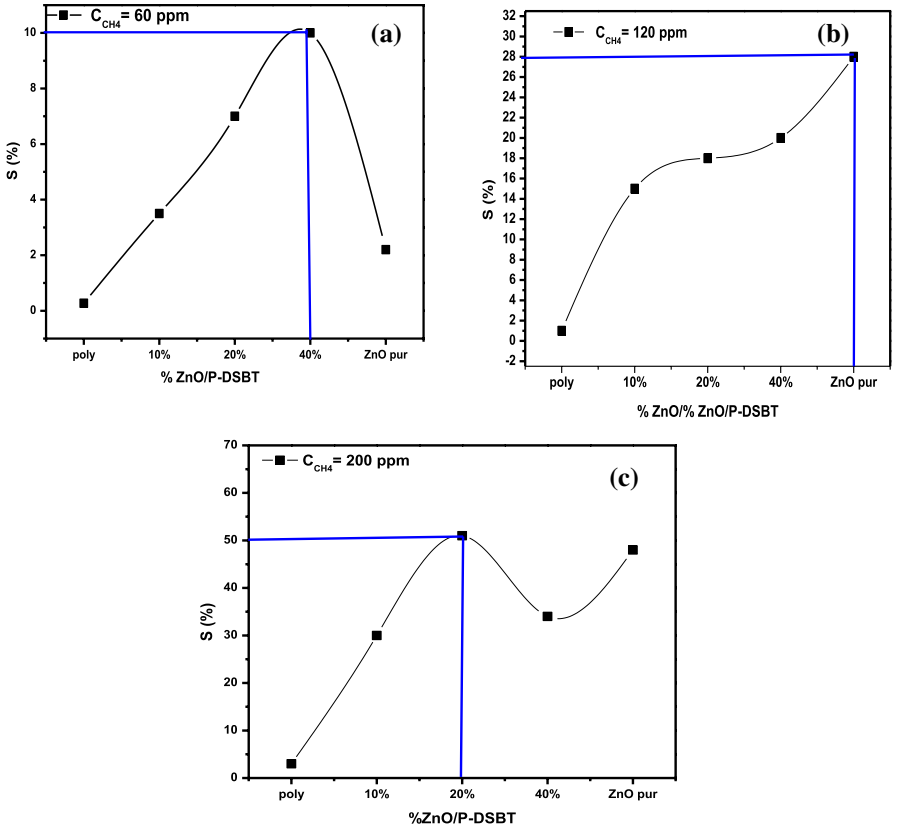

Fig. 12 Variation of the sensitivity as a function of various composite films at 60 ppm (**a**), 120 ppm (**b**) and 200 ppm (**c**)

Region (II) corresponds to the intermediate gas concentration ranges (90 ppm $< C_{CH4} <$ 170 ppm) in which the pure ZnO film exhibits the best sensitivity (Fig. 12b) compared to other hybrid films. In effect, the pure ZnO film is porous (root-mean-square RMS = 89 nm), which facilitates the diffusion of gas [41]. In the case of **P-DSBT/ZnO** materials, the ZnO surface is polymer coated, potentially covering active sites and oxygen species. This may explain why pure ZnO, in this Region (II), exhibits better sensitivity than other hybrid nanocomposites (pure **P-DSBT** and **P-DSBT/ZnO** with different ZnO mass ratios).

Region (III) corresponds to the high gas concentrations ($C_{CH4} >$ 170 ppm), and the **P-DSBT/ZnO**-20% hybrid film exceeds the performance of pure ZnO and has the best sensitivity (Fig. 12c). More generally, the polymer hybrid devices **P-DSBT/ZnO** for different ZnO mass ratios (10%, 20% and 40%) reach a sensitivity value of 30%, 51% and 34%, respectively. There are two reasons for this improvement. First, according to the AFM images, the zinc oxide is well distributed in the polymer

matrix which provides the presence of organic/inorganic interaction (polymer and ZnO). Secondly, an interaction between the p-type **P-DSBT** and the n-type ZnO (p–n junction) generates an electron donor–acceptor system [42]. When the methane gas (donor plus electrons) comes into contact with the nanocomposite, more electrons migrate from the polymer to ZnO, and consequently conductivity and sensitivity increase [43].

Finally, this study has demonstrated that the sensitivity for gas detection has been greatly improved by the interaction of ZnO-based hybrid materials. It should be noted that all the made measurements were carried out at ambient temperature, which explains that the sensitivity levels were below 50%.

Conclusions

During this research work, a novel hybrid **P-DSBT/ZnO** nanocomposite was successfully synthesized by adding homemade ZnO nanoparticles to **a P-DSBT** matrix in different weight percentages (10–100 wt%). Obtained films were successfully prepared on an ITO substrate by a spin coating technique. Atomic force microscopy (AFM) has shown that ZnO nanoparticles are well dispersed in the surface of the nanocomposite formed with (10%, 20% and 40%) ZnO concentrations mass ratios which results in a high surface area. Higher ZnO concentrations mass ratios (> 40%) show the formations of aggregates. This novel hybrid **P-DSBT/ZnO** had shown excellent sensing properties with different ZnO concentrations mass ratios for different methane gas concentrations. For CH_4 gas concentrations less than 90 ppm, the optimal performances (sensitivity equal to 20%) were reached using 20% of ZnO concentrations mass ratio. For CH_4 gas concentrations scaling for 90 ppm to 170 ppm, optimal performances (sensitivity equal to 40%) were seen using **P-DSBT/ZnO**-40% of ZnO concentrations mass ratio. Finally, for high CH_4 gas concentrations scaling from 170 to 220 ppm, an excellent sensitivity equal to 50% is demonstrated using **P-DSBT/ZnO–** 20% of ZnO concentrations mass ratio. Moreover, this hybrid **P-DSBT/ZnO** nanocomposite could be adapted for sensing of other gases, such as hydrogen sulfide (H_2S), ammonia (NH_3) and other hydrocarbon gases.

References

1. Chunshui L, Wei X, Qiuhong Y, Xiaoru W 2019 Micro and Nano Technologies 275–297
2. Dixit S, Srivastava Al, Atul SRK, Shukla, (2007) J Appl Phys 102:113–114
3. Jain S, Karmakar N, Shah A, Shimpi NG (2019) J Mater Sci Eng B 247:114–381
4. Nehal Salahuddin ME, Atsunori M 2021 . J Micro and Nano Technologies 709–731.
5. Patil D, Kolhe K, Potdar HS, Patil P (2021) J Appl Phys 110:124501
6. Ryu H-W, Park B-S, Akbar SA, Lee W-S, Hong K-J, Seo Y-J, Shin D-C, Park J-S, Choi G-P (2003) J Sensors and Actuators B 96:717–722
7. Shouli B, Liangyuanb C, Dianqinga Li, Wensheng Y, Pengcheng Y, Zhiyong L, Aifana C (2010) Chung Chiun Liu. J Sensors Actuators B 146:129–137
8. Akermi M, Sakly N (2013) Rafik Ben Chaabane, Hafedh Ben Ouada. J Mater Sci Semicond Process 16:807–817
9. Bai H, Shi G (2007) J Sensors 7:268–307
10. ElMehdi E, Nejmeddine J, Hafedh BO, Mustapha M. J Appl Phys A. https://doi.org/10.1007/s00339-015-9100-9.
11. Le T-H, Kim Y, Yoon H (2017) J Polymers 9:150

12. Gnanaseelan M, Kalita U, Janke A, Pionteck J, Voit B, Singha NK (2020) J Mater Today Commun 22:100728
13. Singh SP, Sharma SK, Kim DY (2020) J Solid State Sciences 99:106046
14. Saisa, H. Agusnar, Z. Alfian and I. Nainggolan 2020 AIP Conference Proceedings 2267: 020054
15. Aditee Joshi DK, Aswal SK, Gupta JV, Yakhmi and S. A. Gangal, (2009) Appl Phys Lett 94:103115
16. Sanchez C, Julia B, Belleville P, Popall M (2005) J Mater Chem 15:3559–3592
17. Elashmawi IS, Hakeem NA, Marei LK, Hanna FF (2010) J Physica B: Condensed Matter 405:4163–4169
18. Mittal V (2010) J Colloid and Polymer 288:621–630
19. Jaballah N, Chemli M, Fave J-L, Majdo M (2015) J Optical Materials 50:144–153
20. Mahanthesh B, Animasaun IL, Rahimi-Gorji Mohammad, Alarifi Ibrahim M (2019) Physica A: Statistical Mech Appl 535:122471
21. Adesanya Samuel O, Onanaye AS, Adeyemi OG, Rahimi-Gorji Mohammad, Alarifi Ibrahim M (2019) Evaluation of heat irreversibility in couple stress falling liquid films along heated inclined substrate. Journal of Cleaner Production 239:117608
22. Seikh A, Akinbowale AMH, Taheri MR, Gorji NH, Alharthi IK, Khan AR (2019) Physica Scripta 49(12):125218
23. Dutta A, Chattopadhyay H, Yasmin H, Rahimi-Gorji M (2019) Comput Methods Programs Biomedicine 180:105010
24. Abeer Baslem G, Sowmy BJ, Gireesh B.C. Prasannakumara, Rahimi-Gorji Mohammad, Hoang Nguyen Minh (2020) Analysis of thermal behavior of a porous fin fully wetted with nanofluids: convection and radiation. J Mol Liquids 307:112920
25. Alam MW, Bhattacharyya S, Dey BSK, Hammami F, Rahimi-Gorji M, Biswas R (2020) Int Commun Heat Mass Transfer 112:104455
26. Ganesh Kumar K, Abeer Baslem BC, Prasannakumara JM, Mohammad Rahimi-Gorji S, Nadeem, (2020). Microsyst Technol. https://doi.org/10.1007/s00542-020-04792-y
27. Akermi M, Sakly N, Chaabane RB, Ouada HB (2013) J Mater Sci Semiconductor Process 16:807–817
28. ElMehdi E, Nejmeddine J, Hafedh BO, Mustapha Mb J Applied Physics A Materials Science & Processing. 00339–015–9100–9.
29. Sedev R (2011) J Curr Opinion Colloid Interface Sci 16:310–316
30. Lee JS, De Angelis RJ (1996) Nanostruct Mater 7:805
31. Biju V, Neena S, Vrinda V, Salini SL (2008) J Mater Sci 43:1175
32. Mustafa M, Demir M, Koynov K, Akbey Ü, Bubeck C, Park I, I. Lieber wirth, G. Wegner, (2007) J Macromol 40:1089
33. Chougule MA, Dalavi DS, Sawanta Mali PS, Patil AV, Moholkar GL, Agawane J.H. Kim, Shashwati Sen VB, Patil, (2012) J Measurement 45:1989–1996
34. Xiong H-M (2010) J Mater Chem 20:4251–4262
35. Wood F, Samuel IDW, Webster GR, Burn PL (2001) J Synth Met 119:57
36. Zou JP, Le Rendu P, Musa I, Yang SH, Dan Y, Ton That C, Nguyen TP (2011) J Thin Solid Films 519:3997–4003
37. Haider MS, Muhammad Y, Wan Mahmood MY, Ibtisam YA J Mater Sci: Mater Electron DOI https://doi.org/10.1007/s10854-016-5046-8.
38. Yang S, Jiang C, Wei S (2007) J Applied Physics Reviews 4:021304
39. Guo X, Baumgarten M, Müllen K (2013) J Progress in Polymer Science 38:1832–1908
40. Pawar SG, Chougule MA, Raut BT, Shashwati Sen VB, Patil, (2012) J Appl Polym Sci 125:1418–1424
41. Saaedi A, Shabani P, Yousef R (2019) J Alloy Compd 802:335–344
42. Park YBS, Jinc C, Song Y-J, Choi S-W (2019) J Sensors & Actuators: B Chemical 290:467–476
43. Akermi M, Sakly N, Chaabane RB, Ouada HB (2013) J Mater Sci Semiconductor Process 16:807–817